ENGINEERING

Sensing-triggered stiffness-tunable smart adhesives

Duorui Wang[1,2]†, Hong Hu[1,3]†, Shuai Li[1]†, Hongmiao Tian[1]*, Wei Fan[4], Xiangming Li[1,2], Xiaoliang Chen[1,2], Ambrose C. Taylor[4], Jinyou Shao[1,2]*

Artificial dry adhesives have exhibited great potential in the field of robotics. However, there is still a wide gap between bioinspired adhesives and living tissues, especially regarding the surface adaptability and switching ability of attachment/detachment. Here, we propose a sensing-triggered stiffness-tunable smart adhesive material, combining the functions of muscle tissues and sensing nerves rather than traditional biomimetic adhesive strategy that only focuses on structural geometry. Authorized by real-time perception of the interface contact state, conformal contact, shape locking, and active releasing are achieved by adjusting the stiffness based on the magnetorheological effect. Because of the fast switching of the magnetic field, a millisecond-level attachment/detachment response is successfully achieved, breaking the bottleneck of adhesive materials for high-speed manipulation. The innovative design can be applied to any toe's surface structure, opening up a previously unknown avenue for the development of adhesive materials.

INTRODUCTION

Bioinspired dry adhesives have incomparable technical advantages in complex application, such as extraterrestrial manipulation in an extreme space environment, or for ultrathin/fragile/dust-free silicon wafer operation (*1*–*5*). This can be attributed to the uniqueness of dry adhesives to provide strong adhesion, good stability, environmental adaptability, and no damage/pollution to the target surface, which can break the application bottleneck of conventional operation strategies (*6*–*9*). For instance, mechanical clamping requires a matching design of target objects, and sucking with negative pressure can easily lead to stress concentrations. In the past two decades, substantial progress has been made in dry adhesives, which concern the interface action mechanisms (van der Waals forces, negative pressure effect, capillary action, etc.) (*1*, *10*–*12*), fabricating methods (lithography, molding, dipping, etc.) (*13*–*17*), material characteristics optimization (geometrical shapes, material mechanical properties, etc.) (*6*, *18*–*25*), attachment/detachment control methods (contact area control, peeling behavior control, anisotropic structures, etc.) (*4*, *5*, *9*, *26*, *27*), and adhesive devices or systems (self-adhering flexible electronics, climbing robots, manipulation of production line items, etc.) (*28*–*34*).

There is still a wide gap between artificial adhesive materials and living tissues, namely: (i) Surface adaptability. Living organisms can exhibit stable adhesion on flat and uneven surfaces. In contrast, artificial adhesive materials usually exhibit strong adhesion on flat surfaces, which however decreases sharply on uneven surfaces. This can be due to the limited contact area between adhesive materials and target surfaces, which can be further ascribed to the specific shape and contour of the uneven surface. Despite the diverse strategies developed via structural and material optimization (*9*, *13*, *16*, *35*, *36*), the enhancement of adhesion is not notable. (ii) Fast response of attachment/detachment. Natural organisms can quickly crawl over the target surface. By contrast, the switching time of attachment/detachment of adhesive materials is slow (usually at the scale of several minutes). Recently, various methods have been proposed aiming to improve the response time based on approaches such as displacement-speed control (*27*, *37*, *38*) or the use of deformable materials (*4*, *5*, *26*, *27*), etc. Unfortunately, current adhesive materials cannot reach the level of living ones, implying that they cannot be used in high-speed scenarios such as automatic production lines. Thus, it remains a great challenge to develop dry-adhesive materials with both superior surface adaptability and fast adhesion switching capability.

In fact, biological organisms, such as reptiles, can quickly climb on various surfaces without any hesitation regarding the surface texture, material category, and interfacial morphology. In addition to the adhesion of surface microstructures, the excellent climbing ability of reptiles is also inseparable from the active regulation of the muscles and nervous system linked to the toes. More specifically, muscles can instantly change the stiffness of the adhesion system on demand by adjusting the contraction or relaxation state, which is beneficial for soft contact and hard adhesion (i.e., conformal contact and shape locking on target surfaces). Furthermore, the switching ability of attachment and detachment to target surfaces is also enabled by the tunable stiffness of the muscles. That is, a soft-then-hard stiffness state is used for attachment and a sole soft for detachment. This transition of muscle stiffness is usually on the millisecond scale (100 to 500 ms) (*39*, *40*), which provides the rapid adhesion switching ability of the sole to the interface. Another critical factor related to the climbing behavior of reptiles is determining when to soften and when to harden the muscles, which is triggered by the nervous system. Commanded by the interface contact status in real-time detection, reptiles can control the stiffness of muscle systems as well as apply an appropriate mechanical load between toes and target surfaces, achieving conformal contact. Nevertheless, current bioinspired strategies of adhesive materials are isolated by physiological structure or topography, ignoring the tunable stiffness–based active adhesion behavior triggered by contact-state sensing. Although Bartlett and colleagues (*41*) realized target object identification and subsequent adhesion state triggering

[1]Micro-and Nano-Technology Research Center, State Key Laboratory for Manufacturing Systems Engineering, Xi'an Jiaotong University, Xi'an, Shaanxi 710049, China. [2]Frontier Institute of Science and Technology (FIST), Xi'an Jiaotong University, Xi'an, Shaanxi 710049, China. [3]Institute of Textiles and Clothing, The Hong Kong Polytechnic University, Hong Kong SAR, China. [4]Department of Mechanical Engineering, Imperial College London, South Kensington Campus, London SW7 2AZ, UK.
†These authors contributed equally to this work.
*Corresponding author. Email: hmtian@xjtu.edu.cn (H.T.); jyshao@xjtu.edu.cn (J.S.)

process by combining optical sensor and reversible adhesion, there is still a lack of real-time monitoring of mechanical signals of interface adhesion state, which is fundamentally different from contact-state sensing. Therefore, the deficiency on active adhesion impedes the development of adhesive materials with respect to surface adaptability and rapid switching adhesion.

Here, to reduce the wide gap between artificial adhesives and living adhesives, we propose a sensing-triggered stiffness-tunable adhesive controlled by the magnetorheological effect. Such an adhesive achieves the rapid tunable-stiffness effect of functional muscles and senses on the contact status of a perceptron neural network and the interfacial action of epidermis structure, contributing to a new generation of dry adhesives with good adaptability to diverse surfaces and quick attachment/detachment response (Fig. 1). It is noteworthy that the muscle and sensing functions as well as microstructure are integrated into one material, enhancing the overall performance without sacrificing any functional parts.

RESULTS

Design of sensing-triggered stiffness-tunable dry adhesives

For this all-in-one adhesive material, a connected conductive network filled with magnetorheological grease is introduced beneath the adhesive structural layer to mimic the muscle tissue and tactile sensing system functions of reptiles' toes, as well as mushroom-shaped microstructures selected as the adhesive structures (Fig. 1A). As a stiffness-adjustable material, magnetorheological grease has been proved to combine with adhesive structures to achieve switchable adhesion (*42*–*44*). The magnetorheological grease was prepared by mixing ferric oxide and liquid silicone rubber with a mass ratio of 4:1; the detailed fabrication processes are demonstrated in fig. S1. When it is used to contact the target surface, the underlying artificial muscle is in a soft state with the magnetic field off according to the interfacial sensing signals, providing sufficient deformation and contributing to a good adaptability (Fig. 1Bi). Subsequently, it changes immediately from the soft state to the hard state by turning magnetic field on. The abovementioned conformal contact can be frozen rapidly, contributing to a high adhesion strength (Fig. 1B, ii and iii). Then, the artificial muscle can quickly recover to the soft state by removing the magnetic field, which is beneficial for lowering the adhesive force due to the peeling phenomenon on the bonding interface; this is monitored by the interfacial sensing as well (Fig. 1Biv). Moreover, because of the fast variation of the external magnetic field, the response time of switchable adhesion is usually in the millisecond scale, which is sufficient for robotic operation applications. Figure 1C depicts different frozen shapes after contacting in a soft

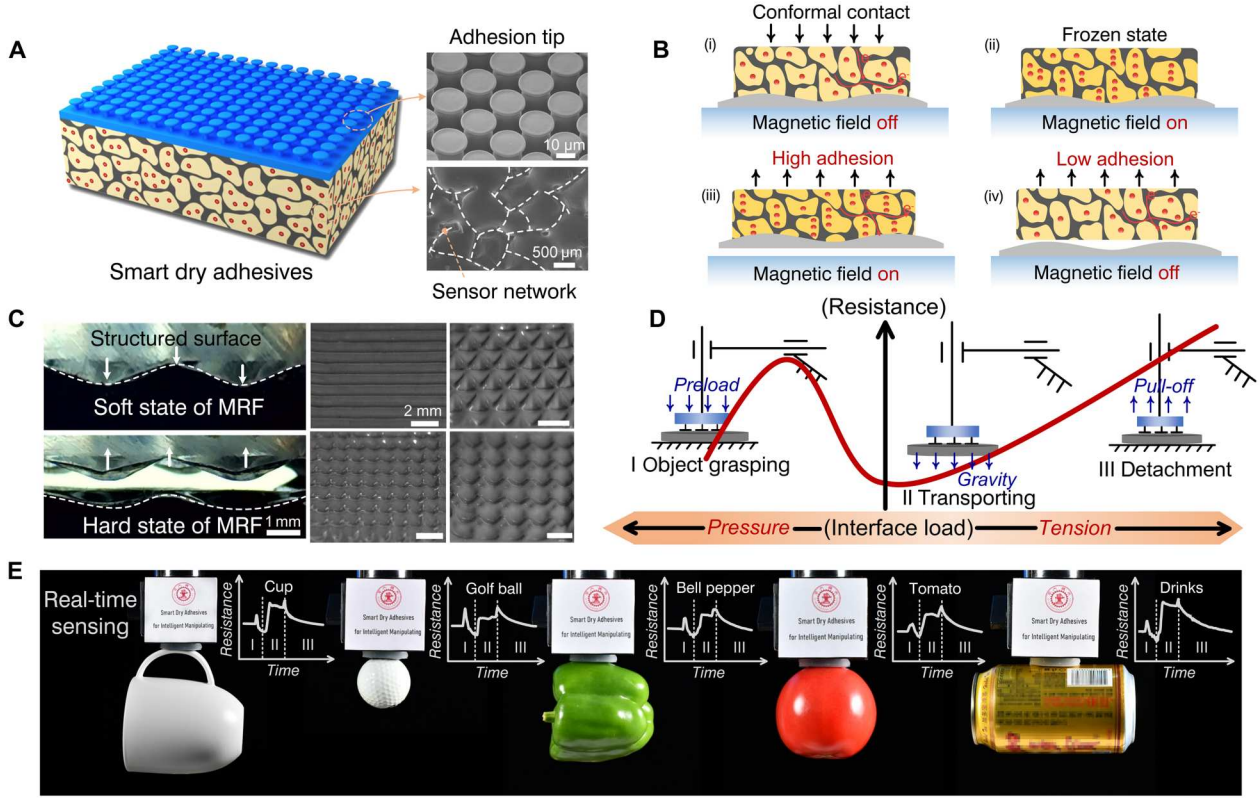

Fig. 1. Illustration of sensing-triggered stiffness-tunable dry adhesives based on the magnetorheological effect. (**A**) Schematic of the all-in-one adhesive material, which contains mushroom-shaped microstructures and a connected conductive network filled with magnetorheological grease. (**B**) Dynamic attachment-detachment process of the adhesive material on nonflat surfaces. (**C**) Frozen shapes of the adhesive material after contacting in a soft state and detaching in a hard state controlled by the magnetic field. (**D**) Schematic diagram of the intelligent operation, in which the variation of resistance can assess the contacting status for safe attachment and stable detachment. (**E**) Surface adaptability and real-time sensing function of the all-in-one material on difficult-to-grasp objects, such as a cup, golf ball, bell pepper, tomato, and drinks can. The real-time change of resistance can be roughly divided into preload (I), grasping, (II) and releasing (III).

state and detaching in a hard state with the magnetic field off/on, indicating a good adaptability on nonflat surfaces. By monitoring the resistance change of the conductive network, which is also used as a container filled with magnetorheological grease for integrated functions of muscle and sensors, one can assess the entire operating process and guide the artificial muscle (soft or hard status) to attach or detach on-demand (Fig. 1D). The red curve refers to the real-time resistance change of the adhesion interface detected by the sensing function during object manipulation. During pressure stage, the sensor presents the characteristic of two phases with the resistance increasing first and then decreasing. Subsequently, in the transporting stage and detachment stage, the resistance of the sensor increases because of the continuous tension caused by the object's gravity and the adhesion. Figure 1E displays some difficult-to-grasp objects, such as a cup, golf ball, bell pepper, tomato, and drinks can, manipulated by the all-in-one adhesive material, highlighting its superior adhesion on various target surfaces and real-time sensing function. The manipulation process of different objects can be roughly divided into preload (I), grasping (II), and releasing (III), and the trend of resistance change in real time is basically consistent with that of Fig. 1D. The detail process of manipulating these objects including picking up and placing down along with the real-time resistance can be seen in fig. S2 and movie S1 in the supporting information.

Adhesion performance

The tunable stiffness of artificial muscle is a critical feature for the surface adaptability of this all-in-one adhesive material. Figure 2A shows the elastic modulus of the synthetic material under different magnetic field strength levels. In the experiments, the magnetic field was applied horizontally and the stiffness was measured vertically (fig. S3). Initially, the elastic modulus of the synthetic material was about 40 kPa. When a magnetic field with a strength of 65 mT was applied, the elastic modulus increased markedly to 700 kPa, i.e., a 20-fold increase in stiffness, transforming from the soft state to a hard state. The increase in stiffness can be attributed to the magnetorheological grease that was confined in the polyurethane network skeleton; that is, besides the so-called magnetorheological effect itself, the skeleton network hinders the flow or deformation of the magnetorheological grease, resulting in a higher stiffness (figs. S4 and S5). In addition, the variation range of stiffness incurred by external magnetic field can be adjusted via changing the material ratio between ferric oxide and liquid silicon rubber. The time-varying stiffness characteristics of the adhesive material affect the adhesion performance essentially through conformal contact and reliable locking, i.e., soft state in the contacting process and hard state in the detachment process. It is evaluated by testing the normal adhesion to the spherical tip with a radius of 5 mm using a load-pull measurement method, in which the sample is firstly brought into contact with the glass sphere probe in a state of magnetic field off (soft state) and then reversely pulls at a speed of 5 mm/min in a state of magnetic field on (hard state) to obtain the value of adhesion. Compared to a dry-adhesive covering with rigid backing, the smart adhesive exhibited a 10-fold increase in the adhesive strength due to the deficiency of the rigid backing for conformal contact (Fig. 2B). Moreover, the adhesion strength of the smart adhesive material is also adjustable with the different magnetic field intensity (fig. S6). Despite that the adhesion force varied because of the contact area changes for the different sphere-shaped probes, the smart adhesive always exhibited an overwhelming advantage compared to a dry adhesive with a rigid backing, by more than one order of magnitude (Fig. 2C). Furthermore, this smart all-in-one adhesive material was also much superior to the adhesive with soft backing, which is a practical and effective way to improve the adhesion performance on nonflat surfaces. The stiffness adjustment of the smart adhesive on-demand is similar to a functionalized muscle rather than the soft backing while keeping the soft state invariably because of the deficiency of the ability to lock the contact state, thus contributing to a further increase in the adhesion strength. Furthermore, this enhancement comes not only from the tunable-stiffness feature of the backing; the mushroom-shaped microstructures also play an important role that can enhance the adhesion when attaching to sphere or complex-shaped indenters (fig. S7).

To investigate the action of stiffness on nonflat surfaces, we recorded the contact status during the entire loading and pulling processes (Fig. 2D). For the material with hard backing, because of the rigid substrate and limited deformation of the surface layer, the area contacting the sphere-shaped probe was quite small (Fig. 2Dii), i.e., point-like contact, which led to poor adhesion. Replacing the backing with a soft material can effectively increase the contact area and increase the adhesion strength accordingly. Nevertheless, different strategies, such as keeping the soft state invariable or switching to a higher-stiffness state in the pulling process, would lead to quite different performances. These differences derive from the changes in the contact state, i.e., whether the conformal contact can be maintained or not (Fig. 2Diii). For the former, the recovery of the soft adhesive in the pulling process decreases the contact area and forms an N-shaped contact at the moment of detaching. For the latter, the U-shaped contact remains almost unchanged during the entire pulling process because of the high stiffness. This constant U-shaped contact in the detachment process provides a relatively large contact area, small peel-off angle, and possible tangential friction, which are all beneficial to improving the adhesion performance. According to the monitoring image at the moment of detaching, the contact area under smart grasping was notably about 23 times larger compared to the soft one, no obvious peeling behavior was observed, and the angle between adhesive material and sphere surface at the contact edge was about 20.89°, far smaller than that in soft detaching (figs. S8 and S9). The hard and conformal contact between the smart adhesive and sphere also changed the detaching behavior mode from normal to hybrid normal tangent. In this situation, the friction in the tangential direction contributes also to the improvement of adhesion strength. In addition, U-shaped deformation can be quickly recovered to the flat shape after magnetic field is removed (fig. S10). Rapid shape locking and recovery also endow the adhesives with good cycling performance (fig. S11).

In some degree, irregular or roughness surface can be regard as combination of numerous protruding probes with different shapes and sizes. Thus, the proposed smart adhesive may have great superiority in grasping these difficult-to-adhesion objects in traditional concept. Figure 2 (E to G) demonstrates the performance of the smart adhesive on rough surface and surfaces with spherical cap, and pyramid structures; the specific dimensions of the uneven surfaces can be found in fig. S12. Although surfaces with different morphologies result in different adhesion strengths, the strength under smart grasping was remarkably improved for all types of surfaces.

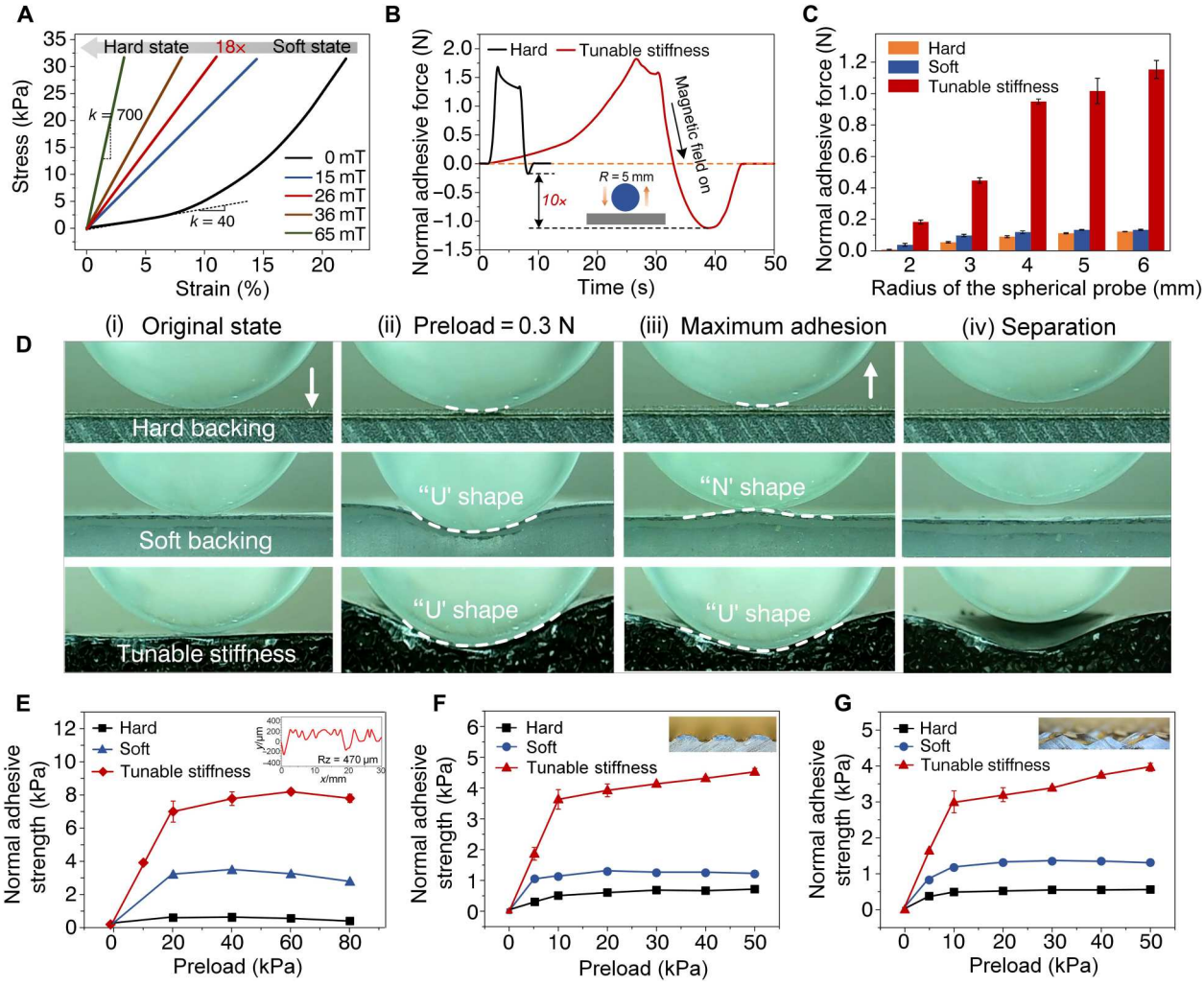

Fig. 2. Adhesion performance of the all-in-one adhesive material. (**A**) Elastic modulus of the synthetic material under different magnetic field magnitudes. (**B**) Adhesive force of the smart adhesive compared with traditional dry-adhesive covering on rigid backing. (**C**) Adhesion of the smart adhesives on sphere-shaped probes with different curvatures compared with dry-adhesives covering on rigid and soft backing. (**D**) Real-time recorded contact states in the entire loading and pulling processes of the smart adhesive and dry adhesives with rigid and soft backings. (**E** to **G**) Adhesion of the smart adhesive material on a rough surface and surfaces with spherical cap and pyramid structures.

The difference in the absolute adhesion strength originates from the change in the contact area; a slowly changing surface topography, such as that with spherical cap structures, is much easier to be contacted conformably and results in a relatively larger adhesion strength (fig. S13).

Adhesion enhancement mechanism

To better understand the tunable-stiffness adhesion enhancing mechanism, we propose a numerical model on the basis of interfacial cohesive zone theory to analyze the contact-separation process for three scenarios (hard, soft, and tunable stiffness). In this model, three stages were adopted to evaluate the adhesive status: stage I, the contact state (moment of the maximum deformation to demonstrate the contact state); stage II, the inversion or pulling state (moment of the reversal interfacial stress to demonstrate the working region on adhesion); and stage III, the separation state (moment of the adhesive material separated from the probe to demonstrate the output adhesive force) (Fig. 3A). The numerically obtained dynamic contacting-separation behavior is presented in movies S2 to S4. Similar to the experimental observations, the contact area of soft and tunable-stiffness adhesive was much larger than that in the hard one, with an identical preload due to the lower elastic modulus (stage I; Fig. 3A). This was accompanied by the evolution of the contact area demonstrated in Fig. 3B. In this stage, the critical parameter was the elastic modulus, determining either point contact (hard backing) or U-shaped contact (soft and tunable stiffness). The latter significantly eliminated the stress concentration in the contact interface, which was beneficial for improving the contact area (Fig. 3C).

In stage II, the interfacial stress changed from compressive to tensile, that is, adhesive force appeared. At this moment, the amount of adhered microstructures is listed as tunable stiffness, soft and hard from greatest to least, which may be a reason behind the superior performance of tunable stiffness. In the soft

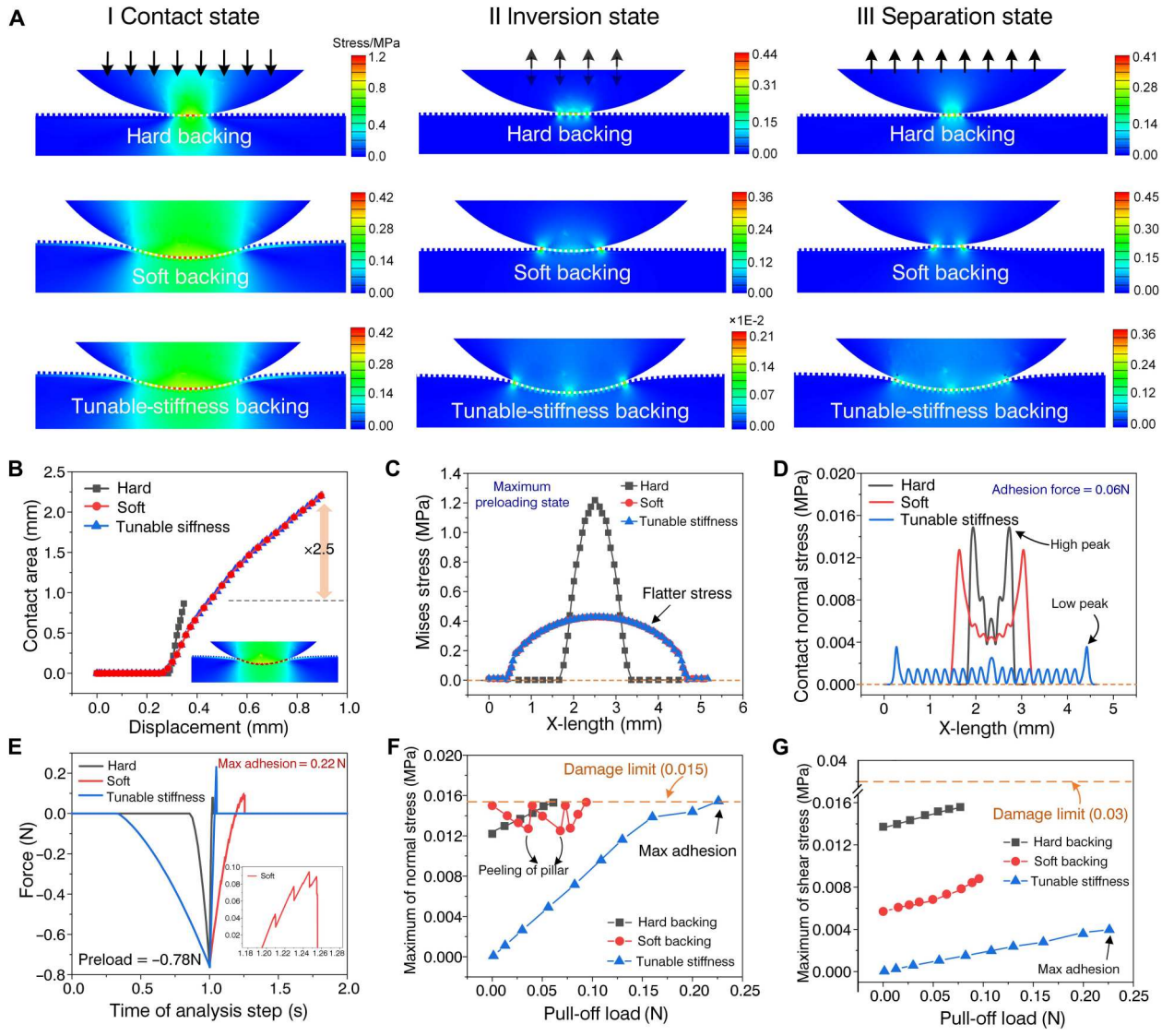

Fig. 3. Adhesion enhancement mechanism of adhesive materials on curved surfaces. (**A**) Stress distribution of soft, hard, and tunable-stiffness backings in the three stages during the contact-separation process. (**B**) Contact area evolution in the attachment process. (**C**) Interfacial distribution of von Mises stress in the contacting region for the three backing cases under maximum deformation. (**D**) Interfacial distribution of normal contact stress in the contacting region under an identical adhesive force. (**E**) Numerical results on adhesive force for the three backing cases. (**F** and **G**) Variation of interfacial stress with pull-load forces for the three backing cases from the maximum normal stress (F) and maximum shear stress (G) perspectives.

and hard cases, the deformation recovery of the different micropillars was not synchronized because of the unequal stored elastic energy of compression on the curved surface, which lead to a large difference in the stress at the bonding interface. On the contrary, in the tunable-stiffness case, the deformed geometry was instantaneously frozen by the applied magnetic field and the elastic energy was "locked." Consequently, the micropillars tend to be stretched as a whole. Here, the stress distribution is listed from good to poor as tunable stiffness and soft and hard backing layer, based on the viewpoint of interfacial equal load sharing (Fig. 3D), which may be another explanation for the experimental results (Fig. 2). In addition, the distribution of the shear contact stress was also flattened because of the tunable-stiffness effects (fig. S17). With the further increase of the pulling distance, the adhered micropillars inevitably began to get damaged, and a crack extended gradually across the entire contact interface, until maximum adhesion force was reached (stage III; Fig. 3A). In this stage, the contact area of the adhesive with soft backing was clearly reduced but was still larger than that of the hard backing, which again emphasizes the importance of the conformal contact induced by a low modulus. In contrast, the contact area of the adhesive with tunable-stiffness backing remained almost unchanged during this process (ideal U-shaped contact). The adhesive force results of the three backing cases are demonstrated in Fig. 3E, which are basically consistent with the experimental results, except of the differentiation lower than the experiments. To save computation time, a two-dimensional model was used for simulation, which is bound to cause the difference between Finite Element

Analysis and experiments. In addition, the reason could also be the difference of contact state between the numerical analysis and the experimental testing, i.e., the former can be considered as an ideal contact, while the latter is often affected by some factors (such as structural defects and test conditions).

In the evolution from stage II to stage III, the interfacial stress, consisting of normal and shear stresses, can be used to deeply understand the adhesive mechanism from the detachment process perspective (Fig. 3, F and G). The soft backing had the highest normal stress and quickly reached the damage threshold value, which triggers the first peeling-off of micropillars (curve decline). Subsequently, its normal stress became lower than that of the hard backing, indicating that its ability to oppose normal damage is superior to that of the hard backing. On the contrary, the normal stress of the tunable-stiffness backing kept increasing linearly at low levels, implying a hindering effect on separation. Similarly, the tunable-stiffness backing maintained the lowest shear interfacial stress with a slowly increasing trend. Because the shear adhesive force of a fiber array is usually larger than the normal one, a damage threshold of the shear stress being larger than the normal one is adopted, in which the shear limit is not reached in the peeling process, leading to the dominant role of the normal stress. If the development of shear stress is faster than that of the normal, then the damage process during crack propagation will be dominated by shear stress. Regardless of the normal and shear threshold, it can be conducted that, compared to the sole soft or hard cases, the tunable stiffness is the most effective approach in adhesion enhancement.

Sensing performance

The real-time monitoring of the contacting status is of particularly importance for the adjustment of the material stiffness through the magnetic field. However, a great challenge on detecting interfacial stress, consisting of compressing and stretching, simultaneously as well as excellent integration with tunable-stiffness function must be overstepped. Inspired by the spider sensory system based on the disconnection-reconnection effect of nanoscale crack junctions, we propose a real-time monitoring sensor using a carbon nanotube (CNT)–based polyurethane network containing magnetorheological grease. To better understand the sensing mechanism of the conductive network, we used CNT-coated fibers, as the basic cells of the network frame, to characterize the sensing performance according to the micro/nanocracks generated through prestretching (fig. S18). Figure 4A demonstrates the variation curve of electric resistance versus prestretching ratio, wherein the resistance changes from 25 kiloohm to 2 megaohm at a prestrain of 5% and further increases to 70 megaohm corresponding to 20%, due to the expansion of CNTs cracks. By removing the external stretch, the electric resistance can quickly recover to its initial value due to the reconnection of cracks. Here, the recovered value was slightly greater than the initial one, which can be possibly attributed to the irregular contact between the crack edges during re-connection (proportional to the number of cracks). Because of the rapid disconnection-reconnection response of micro/nanocracks, the CNT-coated fibers exhibited high linearity for different prestretching ratios (Fig. 4B), which contributed to the easy determination of the applied interfacial force. Here, the effect of prestretching is to create enough cracks on the surface of CNT-network to achieve sensing. The different ratio of prestrain will certainly affect the density and number of cracks, and therefore will change the sensitivity and the actual working range of the sensor. In this work, CNT-networks are only prestretched during the manufacturing process to improve sensitivity, and no further prestretching is required thereafter, including the application of robotic manipulation. The sensitivity of the fibers was positively correlated with the prestretching ratio, which increased from 60 to 320 as the prestretch increased from 5 to 20%. This phenomenon is due to the fact that more cracks are participated in the disconnection-reconnection process. Notably, the sensing measurement range of crack-based fibers in actual applications should not exceed the prior prestretching ratio. If not, the sensitivity of the fibers will fluctuate or even triggering in failure.

The CNT-based conductive network, as a combination of CNT-coated fibers, was also prestretched by a ratio of 20%, which was sufficient for monitoring the attachment and detachment behavior of the adhesive system, to activate the micro/nanocracks for sensing. Subsequently, magnetorheological grease was filled into the conductive network to form the composite structures that integrate the sensing and tunable-stiffness properties. Similar to the electrical response of crack fibers, both the pure and magnetic field–controlled composite conductive network demonstrated a high linearity for tensile load (Fig. 4C). More specifically, the pure conductive network exhibited a sensitivity of roughly 0.035 kPa^{-1}, while that of the composite one was 0.009 kPa^{-1} and 0.006 kPa^{-1} when the magnetic field was on and off, respectively. Although the introduction of the magnetorheological grease would slightly decrease the sensitivity, the crack-based sensing function under the soft or hard states, corresponding to the magnetic field off and on, would not disappear, satisfying the sensing requirements. In detail, the reduced sensitivity can be attributed to the increased elastic modulus of the network that is filled with magnetorheological grease (Fig. 4D), leading to an attenuated deformation and thus decreased crack variation. The tensile modulus of the pure conductive network was 125 kPa, while that of the composite network was 400 and 760 kPa when the magnetic field was on and off, respectively.

Except for the tensile force monitoring used for the detachment process, the ability to monitor the compressive force is more crucial for regulating the stiffness during the attachment process. Therefore, the compressive stress sensing performance of the pure and composite conductive networks was investigated, as shown in Fig. 4 (E and F, respectively). The resistance change ratio ($\Delta R/R_0$) of the pure network increased first and then decreased, exhibiting two apparent stages (Fig. 4E). One of the basic units of a porous grid structure can be approximated as a quadrilateral in original state. When the pressure is small (0 to 4 kPa), the two transverse fibers and the two lateral fibers both bend and deform because of extrusion, which leads to wider cracks in the CNT coating. At this time, the resistance signal increases (stage I). When the pressure increases further (4 to 12 kPa), the transverse fibers come into contact, creating a new conductive path, and the resistance signal tends to decrease (stage II). This two-stage resistance trend has also been found in the study of flexible sensors based on carbon black coatings (*45*). In addition, the compressive stress-stain curve revealed the existence three sections: Sections I and III corresponded to stages I and II of resistance variation, with the pressure range within 0 to 4 kPa and 6 to 12 kPa, respectively. Prominently, section II (4 to 6 kPa) demonstrated a sharp increase for the transition of the network sensors from the crack-dominated state to the contact

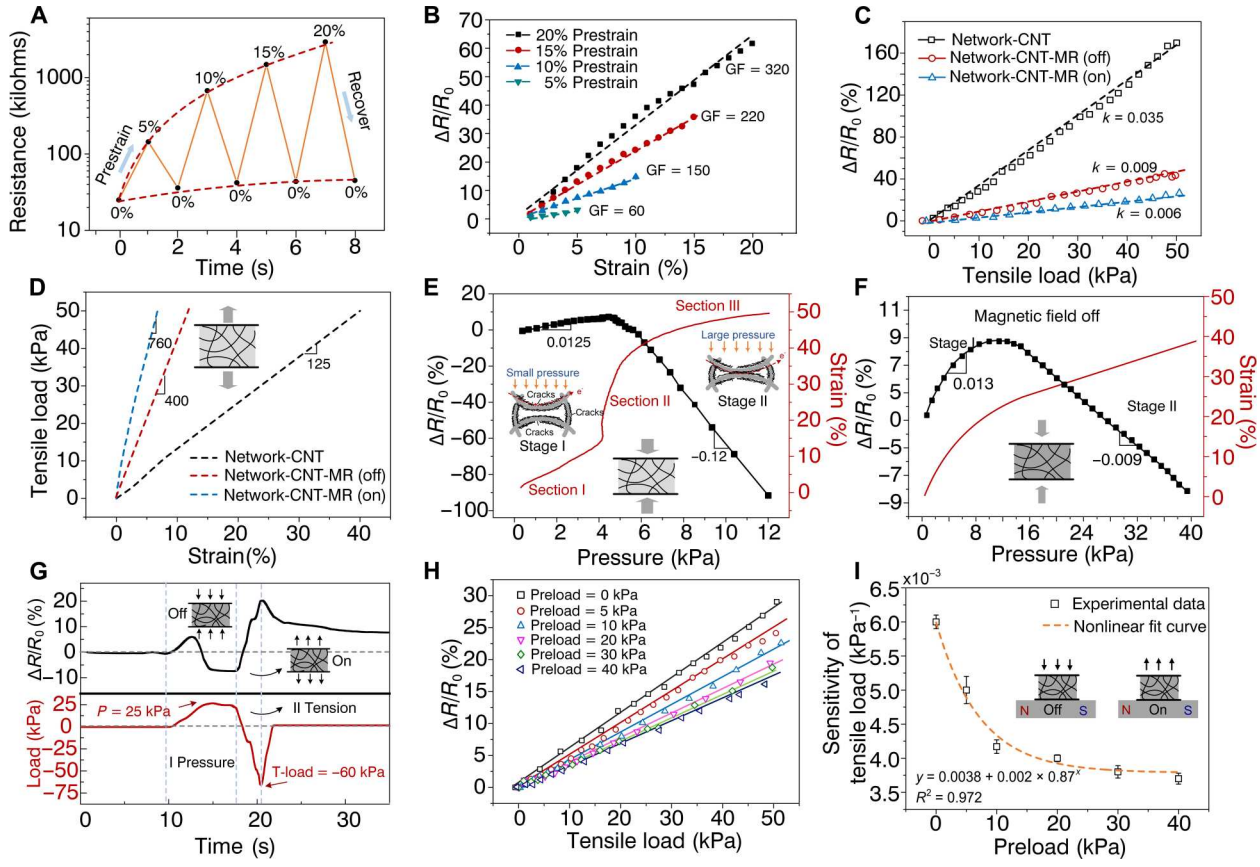

Fig. 4. Sensing performance of the smart dry adhesives for guiding the material's stiffness. (**A**) Variation of the electric resistance in the prestretching process at different stretching ratios of a CNT-coated fiber. (**B**) Sensing function activated by different prestretching ratios. (**C**) Tensile sensing properties of the pure CNT-based conductive network and the composite CNT-based conductive network filled with magnetorheological grease. (**D**) Stress-strain curves of the pure conductive network and the composite conductive network with magnetic field on/off. (**E** and **F**) Compressing sensing and static mechanical properties of the pure conductive network and the composite conductive network with magnetic field off. (**G**) Electric resistance response corresponding to the dynamic attachment/detachment process. (**H**) Sensitivity of the smart adhesives via different preloads under tunable-stiffness state. (**I**) Quantitative relationship between initial preload and tensile load sensitivity.

resistance-dominated state. For the composite network with the magnetic field off (soft-state case), the variations of electrical/mechanical behavior were both similar to those of the pure network. The only difference was that section II of the stress-stain curve disappeared because of the effect of porosity on mechanical behavior after filled with magnetorheological grease (Fig. 4F). In addition to the pressure sensing response to the flat surface, the composite structure also has a discernible sensing performance for curved indenters with different radii (fig. S19), which also meets the contact-state sensing requirements of the smart adhesives when picking up objects with curvatures or complex shapes.

The variation of the electrical resistance during the attachment and detachment processes is clearly discernible; thus, it provides a feasible pathway to monitor the operating motion via solely recording the resistance (Fig. 4G). Hence, a velocity of 2 mm/min was set to manage the probe approaching and contacting the adhesive sample of the composite conductive network until a preload pressure of 25 kPa was reached; then, the contact status was maintained for 2 s. Subsequently, the probe was pulled away from the adhesive sample until it was fully detached. During this procedure, the resistance was initially enhanced and then lowered, which corresponded to the contacting stage. Subsequently, the resistance was maintained as constant as possible, which corresponded to the maintaining stage. Afterward, the resistance was increased and then decreased until it reached a steady state, which coincided with the detachment process. The resistance in the detachment stage increased with increasing tensile stress and exhibited high linearity for different preloads, indicating that the crack propagation was the dominant reaction mechanism (Fig. 4H). There are two reasons for this linearity trend under different preloads. First, the R_0 caused by the pre-preload is different (fig. S20). However, different states of preload change the stiffness of the network, so that the strain is different under the same tensile load (fig. S21). The strain difference affects the tensile degree of the crack and thus changes the resistance rate of the sensor. Furthermore, the quantitative relationship between the preload and tensile response was determined by fitting to the data in the linear region of each curve, i.e., $y = 0.0038 + 0.002 \times 0.87^x$, where y is the tensile load sensitivity and x is the initial preload (Fig. 4I). This provides a criterion for determining the preload pressure and contact status.

Performances of intelligent robotic manipulation

Aside from the real-time monitoring of the interfacial stress, grasping and releasing target surfaces, as well as quick response, are also

required functions. In our case, altering the stiffness can lead to high and low adhesion (i.e., switchable adhesion) controlled by the magnetic field. A spherical probe (R = 6 mm) was used to investigate the material adhesion under tunable stiffness and solely soft state (Fig. 5A), where a 10-fold difference in adhesion was observed. Although there is still a gap between this switch ratio and some current reversible adhesive materials based on stiffness regulation (such as shape memory polymer, thermoplastic polymer, etc.) (*46*, *47*), it can be further improved by changing the magnetic field strength. With the increase of magnetic field intensity, the switch ratio of adhesive can reach nearly 30 (fig. S22). In addition, the proposed tunable-stiffness strategy can achieve the fast response time compared to the approaches with light and thermal control (*5*, *36*, *48*), even reaching the level of pneumatic control. Moreover, the tunable-stiffness regulation method based on magnetic field may have a simper structural configuration compared to the pneumatic control method, which usually requires additional fluid channel design to provide pressure for a controllable pick-and-place system (*9*, *49*, *50*, *51*). The upper limit for grasping objects was determined by the high adhesion, while the lower limit for releasing objects was determined by the low adhesion. This means that, if the target object weight is greater than the upper adhesion limit, then it cannot be gripped, while if the object weight is lower than the lower adhesion limit, then it cannot be released. To determine the safe operating range, we assessed the adhesion range of the adhesive material on the basis of two typical flat and curved surfaces under different preloads (Fig. 5, B and C). The gripping-releasing range increased with the increase of the preload until it became nearly constant. The safe operating range was fixed for a certain preload, corresponding to the largest weight below than the upper adhesion limit and the smallest one above the lower adhesion limit (Fig. 5D).

Using the all-in-one adhesive material, a nonplanar surface (fig. S23) with two 200-g weights attached (Fig. 5E) was successfully gripped, transferred, and released (movie S5). Initially, no pressure signal was recorded, because there was no contact. Then, the adhesive material being in a soft state (magnetic field off) approached the object surface for conformal contact under the action of preload, as indicated by a typical resistance signal representing the contact stage (increased and subsequently decreased). Subsequently, the object was picked up with the magnetic field switched on (hard state), in which the resistance, as a characteristic indicator of the pick-up stage, increased constantly because of the stretching behavior. In the transferring process, the resistance was slightly decreased because of the objects hanging for a lengthy period of time. A slight reduction in the signal indicates that the object has been securely grasped at this stage; otherwise, a sharp increase in the resistance indicates that the object has dropped off from the adhesive sample, which is a judgement criterion for determining the gripping condition. After the object reached the target location, the magnetic field was turned off, resulting in a soft state and triggering a releasing behavior, where the resistance was drastically increased. Here, the response time of the intelligent adhesive material was defined

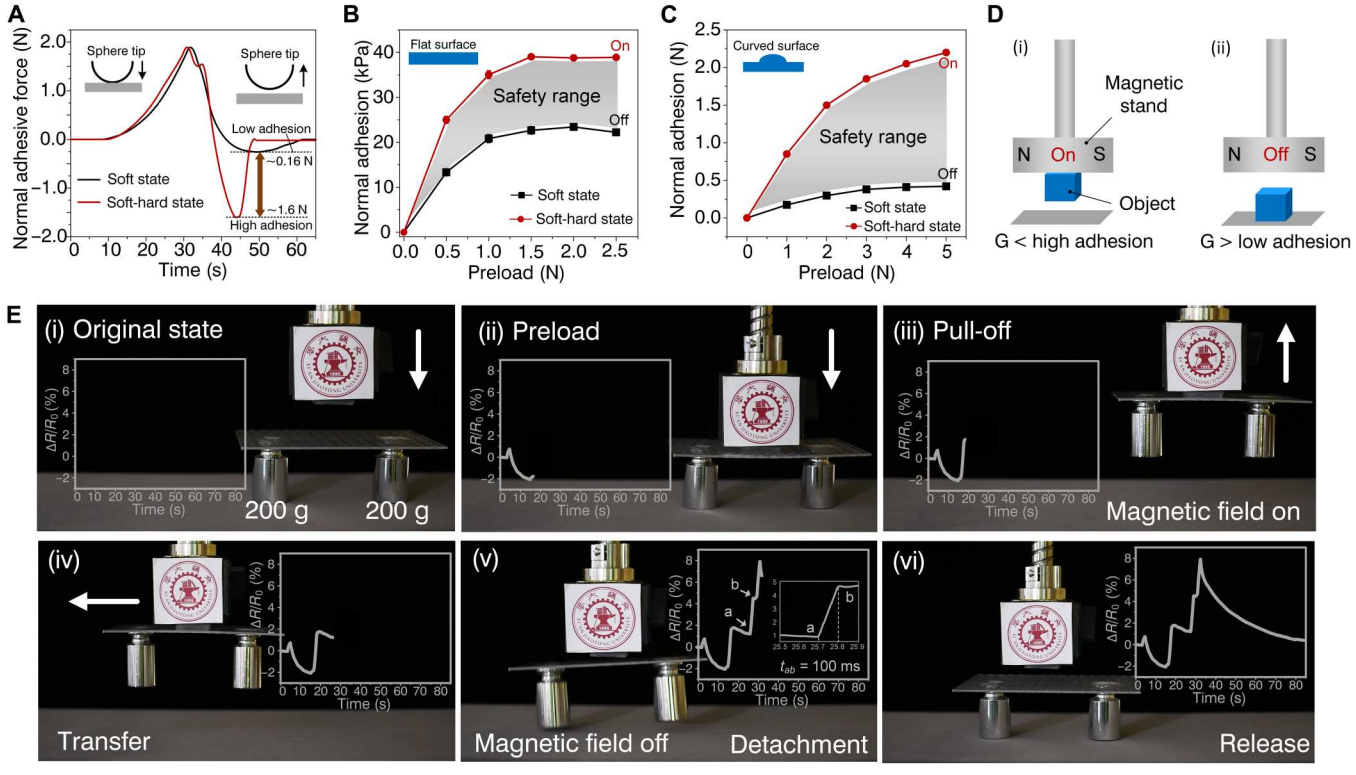

Fig. 5. Demonstration and real-time detection of the smart manipulation process on a nonflat surface with sensing-triggered stiffness-tunable dry adhesives. (**A**) Normal adhesion strength of the material for tunable stiffness and soft state with a spherical probe (R = 6 mm). (**B** and **C**) Safety range of the adhesive material in the manipulation process by measuring the high and low adhesion under different preload levels on a flat surface (B) and a spherical surface (C). (**D**) A control strategy for the intelligent manipulation of smart adhesive materials based on the safety range indicated by sensing signals. (**E**) Complete intelligent manipulation process on a nonflat surface with a weight of 400 g.

as the time required by the resistance to increase from point a to point b (100 ms; inset in Fig. 5Ev). Because of the quick response of the magnetorheological grease to external magnetic fields, the switching time of tunable adhesion is fast (~100 ms), which is comparable to that of the mammalian skeletal muscles and sufficient for robotic manipulation. The subsequent process of interface crack propagation led to a further increase of the resistance after point b. Last, the resistance returned to its original value, indicating that the object was released from the adhesive material. Here, the switching time of adhesives was characterized by recording the corresponding change in resistance characteristics. The conventional experimental characterization method (recording the time of object falling) was also used to characterize the switching time of adhesives, and the result was about 160 ms (fig. S24 and movie S6).

Owing to the matching relationship between the gripping/releasing states and the resistance signals, intelligent operation on various surfaces through smart adhesive materials is achievable, even through some fragile materials that are extremely sensitive to contact loads (fig. S25 and movie S7 in the supporting information). These materials (silicon wafers, ultrathin glass, etc.) play an important role in semiconductor manufacturing, liquid crystal display panel production, and other fields; how to achieve a safe and stable manipulation has been a difficult problem because of their brittleness and fragile characteristics. The manipulation of fragile materials by proposed intelligent adhesive materials based on magnetic field has further expanded the application field of adhesive materials.

DISCUSSION

Inspired by natural active adhesive that owe their excellent properties to muscle tissues, neural networks, and surface microstructures, we proposed a novel smart adhesive strategy of sensing-triggered stiffness-tunable dry adhesives. For this all-in-one adhesive material, a connected conductive network filled with magnetorheological grease is introduced beneath the adhesive structural layer to mimic the muscle tissue and tactile sensing system functions of reptiles' toes, as well as mushroom-shaped microstructures selected as the adhesive structures.

Authorized by the interfacial stress sensing, the stiffness of the magnetorheological grease can be adjusted to be soft (magnetic field off) when approaching the target-object surface for conformal contact, then it can be switched to a hard state (magnetic field on), when picking up the object, and again recover to the soft state when releasing the object. The autonomous deformation and shape locking of the adhesive material provides a relatively large contact area, a small peel-off angle, and a possible tangential friction, which are all beneficial to improving the adhesion performance and enabling the manipulation of various surfaces without considering the surface morphology or texture. Compared to a conventional dry-adhesive covering with rigid backing, the smart adhesive exhibited a 10-fold increase in the adhesive strength due to the deficiency of the rigid backing for conformal contact and have been verified to successfully picking up objects with diverse surfaces typically used in daily life.

On the basis of the interfacial sensing indications, the stiffness can be regulated on demand through the magnetorheological effect to realize the reliable adhesion and capacity to operate swiftly. Owing to the matching relationship between the gripping/releasing states and the resistance signals, intelligent operation on various surfaces through smart adhesive materials is achievable. Furthermore, because of the quick response of the magnetorheological grease to external magnetic fields, the switching time of tunable adhesion is fast (~100 ms), which is comparable to that of the mammalian skeletal muscles and especially beneficial for robotic manipulation with high tempo. In addition, the grasping ability and manipulating range of smart adhesive can be further improved by increasing magnetic field intensity or optimizing the composition of magnetorheological grease.

We suspect that it is a new generation of dry adhesives with good adaptability to diverse target surfaces and quick response of attachment/detachment, which performed from the viewpoint of the smart and active adhesive instead of traditional passive adhesive. Actually, incorporating the sensing-triggered stiffness-tunable functional layer to adhesives is a universal strategy that can be applied to any toe's surface structure, opening up a previously unknown avenue for the creation of smart adhesives for innovative robotic applications including gripping, manipulation, and locomotion.

MATERIALS AND METHODS

Materials

Unless stated otherwise, solvents and chemicals were obtained commercially and used without further purification. Polydimethylsiloxane (PDMS) (Dow Corning Sylgard 184) obtained from Dow Corning Inc. Multiwalled CNTs [7 weight % (wt %)] obtained from XFNANO Co., Ltd. Polyurethane sponge obtained from Hangmei Co., Ltd. Carbonyl iron particles (particle size, 3.6 μm) obtained from Zhongmai Metal Materials Co., Ltd. Ag paste obtained from Lihongjin Technology Co., Ltd. (Shenzhen, China). AB glue (HY-E610) was obtained from Hongyejie Co., Ltd. (Shezhen, China).

Fabrication of sensing network structure

The sensing network structure was prepared by a simple dip-coating process, and the carrier was a PU sponge with a porous network structure. First, the pure PU sponge was cut into 20 mm by 20 mm by 4 mm and placed in deionized water for 10-min ultrasonic cleaning. Subsequently, the PU sponge was treated with oxygen plasma to increase the surface energy of the fiber inside the structure, and the process parameter was 300 W-60 s. Next, the PU sponge was completely immersed in an aqueous solution of multiwalled CNTs with a mass fraction of 10%, until the carbon tubes were completely attached to the surface of the fibers. Then, the soaked PU sponge was placed in an oven at 100°C for 30 min to ensure that the solvent of the carbon tubes solution was completely volatilized. At this time, a dense sensing network was formed inside the structure of the PU sponge. Last, the conductive silver paste was evenly spread on the top and bottom of the sponge and sintered with the copper wire at 130°C for 10 min to form a stable sensing unit.

Fabrication of mushroom-shaped adhesive structure

Mushroom-shaped adhesive structure was made with PDMS through the currently commonly used molding process (*28*, *52*–*54*). Here, the mold was prepared by the double-sided exposure process proposed by our team before (*55*), which can realize the

fabrication of mushroom-shaped structure with controllable structure and good uniformity. The body and the curing agent of the PDMS were mixed and stirred uniformly in a ratio of 10:1 and then poured onto the mold and evacuated for 10 min. Subsequently, spin coating was performed, and the curing was completed in an oven at 80°C for 1 hour. Last, the structure was obtained by demolding. The thickness of backing layer was controlled by change the casting parameters. The mushroom-shape microstructures are about 14 μm in height with a 12 μm in spacing, and the diameter of contact tip and pillar are 18 and 14 μm, respectively.

Fabrication of adhesives sample with different backing

To verify the effectiveness of tunable-stiffness characteristics on the adhesion performance, the adhesive samples with different backing were fabricated. In the process of curing of adhesive layer, the different substrate material is closely adhered to it and heated for curing. Last, as the adhesive layer solidified, the adhesive sample was completed to fabricate by demolding. Three kinds of material was chosen as the backing layer: glass, silicone rubber (E = 100 kPa), and magnetorheological grease composite structure. To maintain consistency, the thickness of the backing was all 40 mm, and the thickness of the adhesive layer was 100 μm.

Fabrication of magnetorheological grease

The carbonyl iron particles with a particle size of 3.6 μm was mixed with the body agent of PDMS at a mass ratio of 4:1 and stirred for 30 min through the magnetometer blender. Subsequently, the mixed material was placed in a vacuum box for 10 min to remove the remaining air bubbles, and the magnetorheological grease with magnetorheological effect was obtained. The tunable-stiffness effect of the magnetorheological grease is realized by a magnetic base, which has the maximum magnetic induction intensity of 73 mT.

Fabrication of all-in-one smart adhesive materials

The PU sponge (thickness of 4 mm) that has a porous shape and network fiber was chosen as the backing layer of the material. Then, the dip-coating method was performed to make multiwalled CNTs (7 wt %) adhere to the network of the sponge. To make the CNTs more firmly adhere to the surface of the sponge skeleton, we treated the sponge with an oxygen plasma treatment to increase its surface energy so that the binding energy between the CNTs and the skeleton is stronger. Next, the magnetorheological grease was poured into the pores of the sponge and evacuated for 20 min, so that the magnetorheological grease completely entered the inside of the sponge structure. Last, we bonded it with the adhesive structure and encapsulated the overall structure to obtain the smart dry-adhesive material (see fig. S1).

Experimental details of demonstrating tunable-stiffness capability

To verify the shape-freezing function of the tunable-stiffness effect, the prepared sample was placed on the stage of the stretching machine, and a nonflat surface with an area of 5 cm by 5 cm was pressed into the sample at a speed of 2 mm/min. Compression process stops when 3 N was reached, the magnetic base under the sample was opened at this time, and the stiffness of the sample would increase instantaneously under the action of the horizontal magnetic field (see fig. S2). Simultaneously, the stretching machine was moved upward at a speed of 2 mm/min until the target surface was completely separated from the sample. The indentation formed on the surface of the sample was recorded by a charge-coupled device (CCD), and the indentation was completely consistent with the contour of the nonflat surface because of the shape freezing effect (see Fig. 1C). Structures with different contours were pressed into the sample in the soft state and separated in the hard state by the same method, and the different indentation shapes were recorded by CCD (see Fig. 1C). Manipulation demonstrations of various difficult-to-grasp objects are achieved by a robotic arm with 4 degrees of freedom (see fig. S14). First, the magnetic base was fixed to the end of the robotic arm, and then the sample was bound to the surface of the magnetic base. The robotic arm was controlled to make the adhesive material in the soft state contact the target object at different speeds, then the magnetic field was applied to make the adhesive material instantly reach the hard state, and lastly the upward movement of the robotic arm was controlled to grasp different objects (see Fig. 1E).

Experimental details of smart manipulating

Smart manipulation was achieved by a robotic arm with 4 degrees of freedom. First, the magnetic base was fixed to the end of the robotic arm, and then the adhesive sample was bound to the surface of the magnetic base. The target object was a nonflat surface with centimeter-level roughness, and a 400-g weight was fixed below the surface (see fig. S14). Through computer programming, the robot arm is controlled to move downward to achieve a common contact with the target object. At this time, the switch of the magnetic base was turned on, and the robot arm is controlled along the y axis to move up; the adhered sample will complete the grasping process of the object. Subsequently, the robotic arm is controlled to move along the x axis to simulate the transfer process of the object. After reaching the designated position, the switch of the magnetic base was closed, the adhesion force drops rapidly because of the soft state, thus completing the release of the object.

Measurements of elastic modulus of synthetic material under different strength of magnetic field

To measure the stiffness change of the material under different magnetic field strengths, we tested its elastic modulus under corresponding conditions. Here, we used the index of compressive stiffness to investigate its elastic modulus. The test process was completed on a pull-pressure test machine (see fig. S2). The indenter is a plane with an area of 25 mm by 25 mm, and the down speed was 5 mm/min. The sensor collects mechanical signals and deformation in real time and then converts it into a stress-strain curve. The elastic modulus value is obtained according to the slope of its linear region.

Measurements of adhesion forces with sphere probe

To characterize the adhesion strength of the adhesive material to the uneven surface, a glass ball with a radius of 6 mm was used as the test target to conduct the adhesion test. The test method adopts the general load-pull mode (*7*, *24*, *36*, *56*), that is, the probe is first contacted with the sample to generate a certain contact area, and then the reverse movement is performed until separation. The maximum tensile force generated before separation was defined as the maximum adhesion force. The test equipment is a computer servo pull-pressure test machine (Baoda, PT-1176, China). First, an adhesive sample with a size of 2 cm by 2 cm is attached to the

surface of the magnetic base, and the magnetic base and the stage are fixed to each other. The stretching equipment moves downward at a speed of 2 mm/min, generates a certain pre-pressure and maintains the pressure for 2 s, and then moves in the opposite direction until the probe and the sample are completely separated, and the time-force curve of the tunable-stiffness adhesive material can be obtained (see Fig. 2B). Adhesion materials based on soft substrates were tested using the same process. To explore the adhesion enhancement effect of variable stiffness effect on different sizes, spherical probes with different radius sizes were contacted with the adhered samples with the same pre-pressure (2 N), and then the maximum adhesion force before separation was recorded for data analysis (see Fig. 2C). A nonflat surface (5 cm by 5 cm) with a typical array structure such as spherical cap structures, pyramid structures was used as the test object, and the adhesion force under different preloads was recorded by controlling the displacement of the computer servo pull-pressure test machine (Baoda, PT-1176, China) (see Fig. 2, E to G).

Measurement of sensing property

The characterization of the sensing performance is achieved by testing the sensitivity of the device. The sensitivity of the sensor can be defined as the ratio of the load to the resistance change rate $[P/(\Delta R/R_0)]$ (*57*–*61*). The specific operation is completed by stretching equipment (see fig. S2), placing the sample above the stage, and connecting the lead-out copper wire to a digital source meter (Keysight, B2912A, USA). The tensile machine compresses and stretches the sample under the control of the computer program, and the source meter will record the resistance change generated by the internal structure of the sample. The applied voltage of source meter is 5 V, and the sampling frequency is 200 Hz. After data processing, the sensitivity curve of the sample can be obtained.

Measurement of the sensing performance of CNT-coated network under different prestrain. First, the four groups of CNT-coated fibers were prestretched respectively in different proportions (5, 10, 15, and 20%) and then released to the relaxed state. The pre-strained CNT-coated fibers were subsequently stretched at different strain (5, 10, 15, and 20%), while real-time resistance changes were tested (Fig. 4B).

Materials characterization

The microstructure of the adhesive material was observed by scanning electron microscopy (SU8010, Hitachi, Japan). The adhesion ability of material was characterized by a computer servo pull-pressure test machine (PT-1176, Baoda, China). The time-varying contact state between the adhesive material and the probe was observed through a digital microscope (RS-500C, Kone, China). The electronic performance of the adhesive material was measured in real time by a pull-pressure test machine with a source meter (Keysight, B2912A, USA). The mechanical properties of the samples are testing by the computer servo pull-pressure test machine (PT-1176, Baoda, China).

Supplementary Materials

This PDF file includes:

Supplementary Text
Figs. S1 to S26
Tables S1 and S2
Legends for movies S1 to S7

Other Supplementary Material for this manuscript includes the following:

Movies S1 to S7

REFERENCES AND NOTES

1. K. Autumn, Y. A. Liang, S. T. Hsieh, W. Zesch, W. P. Chan, T. W. Kenny, R. Fearing, R. J. Full, Adhesive force of a single gecko foot-hair. *Nature* **405**, 681–685 (2000).
2. A. K. Geim, S. V. Dubonos, I. V. Grigorieva, K. S. Novoselov, A. A. Zhukov, S. Y. Shapoval, Microfabricated adhesive mimicking gecko foot-hair. *Nat. Mater.* **2**, 461–463 (2003).
3. J. Hao, E. W. Hawkes, C. Fuller, M. A. Estrada, S. A. Suresh, N. Abcouwer, A. K. Han, S. Wang, C. J. Ploch, A. Parness, M. R. Cutkosky, A robotic device using gecko-inspired adhesives can grasp and manipulate large objects in microgravity. *Sci. Robot.* **2**, eaan4545 (2017).
4. H. Shahsavan, S. M. Salili, A. Jakli, B. Zhao, Thermally active liquid crystal network gripper mimicking the self-peeling of gecko toe pads. *Adv. Mater.* **29**, 1604021 (2017).
5. E. Kizilkan, J. Strueben, A. Staubitz, S. N. Gorb, Bioinspired photocontrollable microstructured transport device. *Sci. Robot.* **2**, eaak9454 (2017).
6. L. Heepe, S. N. Gorb, Biologically inspired mushroom-shaped adhesive microstructures. *Annu. Rev. Mat. Res.* **44**, 173–203 (2014).
7. S. Gorb, M. Varenberg, A. Peressadko, J. Tuma, Biomimetic mushroom-shaped fibrillar adhesive microstructure. *J. R. Soc. Interface* **4**, 271–275 (2007).
8. E. Arzt, S. Gorb, R. Spolenak, From micro to nano contacts in biological attachment devices. *Proc. Natl. Acad. Sci. U.S.A.* **100**, 10603–10606 (2003).
9. S. Song, D. M. Drotlef, C. Majidi, M. Sitti, Controllable load sharing for soft adhesive interfaces on three-dimensional surfaces. *Proc. Natl. Acad. Sci. U.S.A.* **114**, E4344–E4353 (2017).
10. W. Sun, P. Neuzil, T. S. Kustandi, S. Oh, V. D. Samper, The nature of the gecko lizard adhesive force. *Biophys. J.* **89**, L14–L17 (2005).
11. G. Huber, H. Mantz, R. Spolenak, K. Mecke, K. Jacobs, S. N. Gorb, E. Arzt, Evidence for capillarity contributions to gecko adhesion from single spatula nanomechanical measurements. *Proc. Natl. Acad. Sci. U.S.A.* **102**, 16293–16296 (2005).
12. K. Autumn, M. Sitti, Y. A. Liang, A. M. Peattie, W. R. Hansen, S. Sponberg, T. W. Kenny, R. Fearing, J. N. Israelachvili, R. J. Full, Evidence for van der Waals adhesion in gecko setae. *Proc. Natl. Acad. Sci. U.S.A.* **991**, 12252–12256 (2002).
13. D. M. Drotlef, M. Amjadi, M. Yunusa, M. Sitti, Bioinspired composite microfibers for skin adhesion and signal amplification of wearable sensors. *Adv. Mater.* **29**, 1701353 (2017).
14. D. Tao, X. Gao, H. Lu, Z. Liu, Y. Li, H. Tong, N. Pesika, Y. Meng, Y. Tian, Controllable anisotropic dry adhesion in vacuum: Gecko inspired wedged surface fabricated with ultraprecision diamond cutting. *Adv. Funct. Mater.* **27**, 1606576 (2017).
15. D. Brodoceanu, C. T. Bauer, E. Kroner, E. Arzt, T. Kraus, Hierarchical bioinspired adhesive surfaces-a review. *Bioinspir. Biomim.* **11**, 051001 (2016).
16. H. E. Jeong, J. K. Lee, N. K. Hong, H. M. Sang, K. Y. Suh, A nontransferring dry adhesive with hierarchical polymer nanohairs. *Proc. Natl. Acad. Sci. U.S.A.* **106**, 5639–5644 (2009).
17. H. Hu, H. Tian, X. Li, J. Shao, Y. Ding, H. Liu, N. An, Biomimetic mushroom-shaped microfibers for dry adhesives by electrically induced polymer deformation. *ACS Appl. Mater. Interfaces* **6**, 14167–14173 (2014).
18. S. C. Fischer, E. Arzt, R. Hensel, Composite pillars with a tunable interface for adhesion to rough substrates. *ACS Appl. Mater. Interfaces* **9**, 1036–1044 (2017).
19. Z. Wang, Slanted functional gradient micropillars for optimal bioinspired dry adhesion. *ACS Nano* **12**, 1273–1284 (2018).
20. Z. Ye, G. Z. Lum, S. Song, S. Rich, M. Sitti, Phase change of gallium enables highly reversible and switchable adhesion. *Adv. Mater.* **28**, 5088–5092 (2016).
21. A. G. Gillies, J. Kwak, R. S. Fearing, Controllable particle adhesion with a magnetically actuated synthetic gecko adhesive. *Adv. Funct. Mater.* **23**, 3256–3261 (2013).
22. C. G. Ara'nzazu del Campo, E. Arzt, Contact shape controls adhesion of bioinspired fibrillar surfaces. *Langmuir* **23**, 10235–10243 (2007).
23. S. Gorumlu, B. Aksak, Sticking to rough surfaces using functionally graded bio-inspired microfibres. *R. Soc. Open Sci.* **4**, 161105 (2017).
24. Q. Liu, D. Tan, F. Meng, B. Yang, Z. Shi, X. Wang, Q. Li, C. Nie, S. Liu, L. Xue, Adhesion enhancement of micropillar array by combining the adhesive design from gecko and tree frog. *Small* **17**, e2005493 (2021).
25. M. P. Murphy, B. Aksak, M. Sitti, Gecko-inspired directional and controllable adhesion. *Small* **5**, 170–175 (2009).
26. S. Song, M. Sitti, Soft grippers using micro-fibrillar adhesives for transfer printing. *Adv. Mater.* **26**, 4901–4906 (2014).
27. K. Jin, J. C. Cremaldi, J. S. Erickson, Y. Tian, J. N. Israelachvili, N. S. Pesika, Biomimetic bidirectional switchable adhesive inspired by the gecko. *Adv. Funct. Mater.* **24**, 574–579 (2013).

28. T. Kim, J. Park, J. Sohn, D. Cho, S. Jeon, Bioinspired, highly stretchable, and conductive dry adhesives based on 1D-2D hybrid carbon nanocomposites for all-in-one ECG electrodes. *ACS Nano* **10**, 4770–4778 (2016).
29. C. Pang, J. H. Koo, A. Nguyen, J. M. Caves, M. G. Kim, A. Chortos, K. Kim, P. J. Wang, J. B. H. Tok, Z. Bao, Highly skin-conformal microhairy sensor for pulse signal amplification. *Adv. Mater.* **27**, 634–640 (2015).
30. S. Kim, M. Spenko, S. Trujilo, B. Heyneman, D. Santos, M. Cutkosky, Smooth vertical surface climbing with directional adhesion. *IEEE Trans. Robot.* **24**, 65–74 (2008).
31. C. Linghu, S. Zhang, C. Wang, K. Yu, C. Li, Y. Zeng, H. Zhu, Z. You, J. Song, Universal SMP gripper with massive and selective capabilities for multiscaled, arbitrarily shaped objects. *Sci. Adv.* **6**, eaay5120 (2020).
32. S. D. de Rivaz, B. Goldberg, N. Doshi, K. Jayaram, J. Zhou, R. J. Wood, Inverted and vertical climbing of a quadrupedal microrobot using electroadhesion. *Sci. Robot.* **3**, eaau3038 (2018).
33. C. Linghu, C. Wang, N. Cen, J. Wu, Z. Lai, J. Song, Rapidly tunable and highly reversible bio-inspired dry adhesion for transfer printing in air and a vacuum. *Soft Matter* **15**, 30–37 (2018).
34. W. Ruotolo, D. Brouwer, M. R. J. S. R. Cutkosky, From grasping to manipulation with gecko-inspired adhesives on a multifinger gripper. *Sci. Robot.* **6**, eabi9773 (2021).
35. M. Rohrig, M. Thiel, M. Worgull, H. Holscher, 3D direct laser writing of nano- and micro-structured hierarchical gecko-mimicking surfaces. *Small* **8**, 3009–3015 (2012).
36. D. Tan, X. Wang, Q. Liu, K. Shi, B. Yang, S. Liu, Z.-S. Wu, L. Xue, Switchable adhesion of micropillar adhesive on rough surfaces. *Small* **15**, e1904248 (2019).
37. P. Y. Isla, E. Kroner, A novel bioinspired switchable adhesive with three distinct adhesive states. *Adv. Funct. Mater.* **25**, 2444–2450 (2015).
38. J. Purtov, M. Frensemeier, E. Kroner, Switchable adhesion in vacuum using bio-inspired dry adhesives. *ACS Appl. Mater. Interfaces* **7**, 24127–24135 (2015).
39. J. E. Desmedt, E. J. N. Godaux, Fast motor units are not preferentially activated in rapid voluntary contractions in man. *Nature* **267**, 717–719 (1977).
40. M. Li, A. Pal, A. Aghakhani, A. Pena-Francesch, M. Sitti, Soft actuators for real-world applications. *Nat. Rev. Mater.* **7**, 235–249 (2022).
41. S. T. Frey, A. B. M. T. Haque, R. Tutika, E. V. Krotz, C. Lee, Octopus-inspired adhesive skins for intelligent and rapidly switchable underwater adhesion. *Sci. Adv.* **8**, eabq1905 (2022).
42. J. Krahn, E. Bovero, C. Menon, Magnetic field switchable dry adhesives. *ACS Appl. Mater. Interfaces* **7**, 2214–2222 (2015).
43. J. Risan, A. B. Croll, F. Azarmi, Compliance switching for adhesion control. *J Polym Sci B* **53**, 48–57 (2015).
44. P. Testa, B. Chappuis, S. Kistler, R. W. Style, L. J. Heyderman, E. R. Dufresne, Switchable adhesion of soft composites induced by a magnetic field. *Soft Matter* **16**, 5806–5811 (2020).
45. X. Wu, Y. Han, X. Zhang, Z. Zhou, C. Lu, Large-area compliant, low-cost, and versatile pressure-sensing platform based on microcrack-designed carbon black@polyurethane sponge for human–machine interfacing. *Adv. Funct. Mater.* **26**, 6246–6256 (2016).
46. A. B. Croll, N. Hosseini, M. D. Bartlett, Switchable adhesives for multifunctional interfaces. *Adv. Mater. Technol.* **4**, 1900193 (2019).
47. A. Luo, S. S. Pande, K. T. Turner, Versatile adhesion-based gripping via an unstructured variable stiffness membrane. *Soft Robot.* **9**, 1177–1185 (2022).
48. M. Tatari, A. Mohammadi Nasab, K. T. Turner, W. Shan, Dynamically tunable dry adhesion via subsurface stiffness modulation. *Adv. Mater. Interfaces* **5**, 1800321 (2018).
49. A. Carlson, S. Wang, P. Elvikis, P. M. Ferreira, Y. Huang, J. A. Rogers, Active, programmable elastomeric surfaces with tunable adhesion for deterministic assembly by transfer printing. *Adv. Funct. Mater.* **22**, 4476–4484 (2012).
50. G. Wan, Y. Tang, K. T. Turner, T. Zhang, W. Shan, Tunable dry adhesion of soft hollow pillars through sidewall buckling under low pressure. *Adv. Funct. Mater.* **33**, 2209905 (2022).
51. M. D. Swift, C. B. Haverkamp, C. J. Stabile, D. Hwang, R. H. Plaut, K. T. Turner, D. A. Dillard, M. D. Bartlett, Active membranes on rigidity tunable foundations for programmable, rapidly switchable adhesion. *Adv. Mater. Technol.* **5**, 2000676 (2020).
52. S. M. Kang, Bioinspired design and fabrication of green-environmental dry adhesive with robust wide-tip shape. *Int. J. Pr. Eng. Manf. Green Technol.* **3**, 189–192 (2016).
53. D. Sameoto, C. Menon, A low-cost, high-yield fabrication method for producing optimized biomimetic dry adhesives. *J. Micromech. Microeng.* **19**, 115002 (2009).
54. D. Sameoto, C. Menon, Direct molding of dry adhesives with anisotropic peel strength using an offset lift-off photoresist mold. *J. Micromech. Microeng.* **19**, 115026 (2009).
55. Y. Wang, H. Hu, J. Shao, Y. Ding, Fabrication of well-defined mushroom-shaped structures for biomimetic dry adhesive by conventional photolithography and molding. *ACS Appl. Mater. Interfaces* **6**, 2213–2218 (2014).
56. M. P. Murphy, S. Kim, M. Sitti, Enhanced adhesion by gecko-inspired hierarchical fibrillar adhesives. *ACS Appl. Mater. Interfaces* **1**, 849–855 (2009).
57. S. Gong, W. Schwalb, Y. Wang, Y. Chen, Y. Tang, J. Si, B. Shirinzadeh, W. Cheng, A wearable and highly sensitive pressure sensor with ultrathin gold nanowires. *Nat. Commun.* **5**, 3132 (2014).
58. G. Schwartz, B. C. K. Tee, J. Mei, A. L. Appleton, D. H. Kim, H. Wang, Z. Bao, Flexible polymer transistors with high pressure sensitivity for application in electronic skin and health monitoring. *Nat. Commun.* **4**, 1859 (2013).
59. S. C. B. Mannsfeld, B. C.-K. Tee, R. M. Stoltenberg, C. V. H.-H. Chen, S. Barman, B. V. O. Muir, A. N. Sokolov, C. Reese, Z. Bao, Highly sensitive flexible pressure sensors with micro-structured rubber dielectric layers. *Nat. Mater.* **9**, 859–864 (2010).
60. C. M. Boutry, Y. Kaizawa, B. C. Schroeder, A. Chortos, A. Legrand, Z. Wang, J. Chang, P. Fox, Z. Bao, A stretchable and biodegradable strain and pressure sensor for orthopaedic application. *Nat. Electron.* **1**, 314–321 (2018).
61. S. Lee, A. Reuveny, J. Reeder, S. Lee, H. Jin, Q. Liu, T. Yokota, T. Sekitani, T. Isoyama, Y. Abe, Z. Suo, T. Someya, A transparent bending-insensitive pressure sensor. *Nat. Nanotechnol.* **11**, 472–478 (2016).

Acknowledgments

Funding: This work was supported by National Natural Science Foundation of China grant 52025055. National Natural Science Foundation of China grant 52175546 and the Fundamental Research Funds for the Central Universities of China grant no. xhj032021016-01. **Author contributions:** Conceptualization: J.S., H.T., and D.W. Methodology: H.T., D.W., H.H., S.L., X.C., and X.L. Investigation: D.W., H.T., H.H., S.L., and X.C. Visualization: D.W., H.T., S.L., and H.H. Numerical simulation: D.W., W.F., A.C.T., and H.T.. Funding acquisition: J.S. and H.T. Project administration: J.S. and H.T. Supervision: J.S. and A.C.T. Writing—original draft: D.W. and H.T. Writing—review and editing: H.T., J.S., and A.C.T. **Competing interests:** The authors declare that they have no competing interests. **Data and materials availability:** All data needed to evaluate the conclusions in the paper are present in the paper and/or the Supplementary Materials.

Submitted 19 October 2022
Accepted 13 February 2023
Published 15 March 2023
10.1126/sciadv.adf4051